

Strongly anisotropic high-temperature Fermi surface of the Kondo semimetal CeNiSn revealed by angle-resolved photoemission spectroscopy

Cédric Bareille,^{1,*} T.-S. Nam,^{2,†} Toshiro Takabatake,³ Kenta Kuroda,¹ Takeshi Yajima,¹ Mitsuhiro Nakayama,¹ So Kunisada,¹ Shuntaro Akebi,¹ Masato Sakano,⁴ Shunsuke Sakuragi,¹ Ryo Noguchi,¹ Byung Il Min,² Shik Shin,¹ and Takeshi Kondo¹

¹*ISSP, The University of Tokyo, Kashiwa, Chiba 277-8581, Japan*

²*Department of Physics, POSTECH, Pohang 37673, Korea*

³*Graduate School of Advanced Sciences of Matter, Hiroshima University, Higashi-Hiroshima 739-8530, Japan*

⁴*Quantum-Phase Electronics Center and Department of Applied Physics, The University of Tokyo, Hongo, Tokyo 113-8656, Japan*



(Received 31 March 2019; revised manuscript received 17 May 2019; published 23 July 2019)

The semimetallic behavior of the so-called “failed Kondo insulator” CeNiSn has been ascribed to a nodal line in the Kondo hybridization derived from a particular symmetry of the Ce $4f$ orbitals ground state. Here we investigate the geometry of the CeNiSn conduction band by combined angle-resolved photoemission spectroscopy (ARPES) in the high-temperature regime and Open core generalized gradient approximation plus spin-orbit coupling calculations, in order to determine how the nodal hybridization takes place. We identify the Fermi sheet involved in the semimetallic regime from its locus and its shape, respectively, in agreement with the expected nodal line and with quantum oscillations. We further extrapolate and discuss the low-temperature Fermi surface in terms of the expected nodal hybridization with a localized f -level. The obtained hypothetical low-temperature Fermi surface is compatible with the description from quantum oscillations, and with both the highly anisotropic magnetoresistance and the isotropic Nernst effect. This work offers an overview of the conduction band of CeNiSn before hybridization, and it paves the way to a definitive understanding of its low-temperature state. In addition, this work serves as a basis for more challenging low-temperature ARPES measurements.

DOI: [10.1103/PhysRevB.100.045133](https://doi.org/10.1103/PhysRevB.100.045133)

I. INTRODUCTION

CeNiSn is a heavy-fermion system with a moderate Sommerfeld coefficient of about $40 \text{ mJ mol}^{-1} \text{ K}^{-2}$ [1,2], and a Kondo scale estimated at $T_K \approx 54 \text{ K}$ [3]. The coherence is set below $T_{\text{coh}} \approx 9 \text{ K}$ as indicated by a positive peak in the Hall resistivity [4]. Earlier transport measurements of CeNiSn evidenced a diverging resistivity at low temperature [5,6], below a drop concomitant to the onset of coherence. Therefore, it was thought to be a small gap Kondo insulator, in other words a Kondo semiconductor. Nevertheless, with the improvement in sample quality, it was later found that the resistivity does not diverge and forms a plateau [7]. Nuclear magnetic resonance measurements show that the opening of a gap through the crossover at T_{coh} leads to a V-shaped density of states in the vicinity of the Fermi level [8,9]. The same conclusions are drawn from break-junction tunneling measurements [10,11]. The measurements also show the suppression of the gap when a modest magnetic field is applied along the a -axis, driving the system to a more common metallic heavy Fermi liquid [11]. Additionally, magnetoresistance was found to show highly anisotropic behavior [12].

All of these observations are likely explained by an anisotropic Kondo hybridization with a node along the a -axis.

The Kondo hybridization is usually assumed to be isotropic, opening an indirect gap over the entire Brillouin zone. Depending on the filling of the f -level, this hybridization may then give rise to a heavy Fermi liquid or to an insulator, respectively, illustrated by Figs. 1(a) and 1(b). The existence of a nodal line along which the hybridization potential is suppressed will prevent the opening of a gap into the density of states. Figure 1(c) illustrates this case: A Fermi surface will remain with a highly anisotropic mass distribution.

In CeNiSn, a nodal line in the hybridization potential is expected to appear along the a -axis from the symmetry of the Ce $4f$ -orbital ground state [13–16]. This particular symmetry was recently confirmed experimentally to be in adequate agreement with the theory, thanks to polarization-dependent x-ray absorption spectroscopy [17]. Nernst effect measurements support the above picture based upon its isotropy [18]. Indeed, they rule out the possibility of a highly anisotropic Fermi pocket, and they leave only the anisotropic effective-mass distribution to explain the observed magnetoresistance, hence supporting the existence of a nodal hybridization.

Finally, Shubnikov–de Haas (SdH) measurements reveal a sole Fermi sheet with the shape of a concave lens, the axis of which is parallel to the a -axis [19]. A comparison of the estimated carrier density with that inferred by the Hall effect of 1.2×10^{-3} electrons/Ce concludes that, at low temperature, there should not be any significant additional Fermi sheet that SdH measurements could not detect. Therefore, the reported sheet should be the main part of the Fermi surface,

*bareille@issp.u-tokyo.ac.jp

†These authors contributed equally to this work.

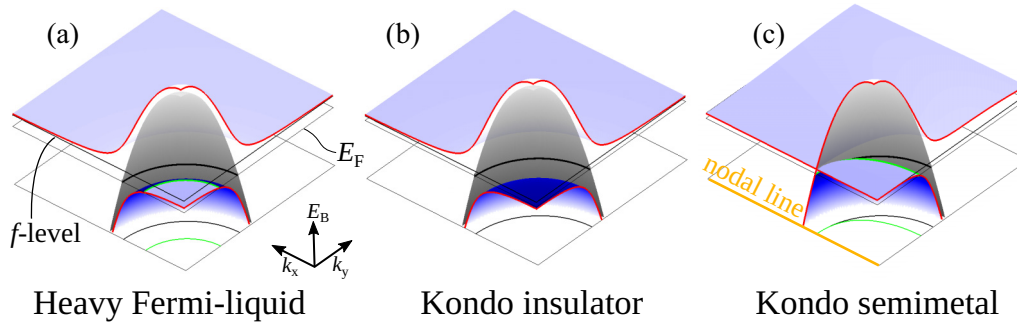


FIG. 1. Kondo hybridization of a holelike conduction band with a localized f -level. The Fermi surface at high temperature (without hybridization) and at low temperature is drawn at the bottom of each graph. Different scenarios give rise to different ground states: (a) Heavy Fermi liquid. (b) Insulator. (c) Semimetal.

and it should be of electron character. Yet, the estimated Sommerfeld coefficient from this sole Fermi sheet is one order of magnitude smaller than the directly measured one; either this discrepancy supports the two-fluid alternative model [20], or an additional extremely heavy Fermi sheet contributes. In fact, inelastic neutron scattering (INS) performed on Pt- and Cu-doped CeNiSn [21,22] nullifies the former hypothesis with a first crystal electric field (CEF) excitation at about 0.02 eV, much higher than the Kondo scale.

Most recently, in the same way as SmB₆ has been qualified as a topological Kondo insulator candidate [23,24], plateaus in the low-temperature resistivity of CeNiSn have been reinterpreted as a possible signature of topologically protected surface states. Because of the particular nonsymmorphic symmetry of CeNiSn, these surface states would show novel Möbius braiding, potentially observable by angle-resolved photoemission spectroscopy (ARPES) [25]. The present work focuses on bulk properties; the bulk electronic structure we report will be of use for future ARPES studies seeking predicted topologically protected surface states.

In all the theoretical and experimental works described above, the characteristics of Kondo hybridization are inferred from f -orbital ground-state symmetry alone. They overlook the role of conduction-band geometry by adopting a simplistic description of it. To clearly determine which Fermi surface would result from the expected anisotropic hybridization at low temperature, to confirm its adequate agreement with previous interpretations, and to shed light upon the relatively high specific heat, a realistic description of the conduction band is needed. Earlier density-functional-theory (DFT) calculations and photoemission spectroscopy (PES) were used to investigate the realistic electronic band structure of CeNiSn. The linear (spin)-density approximation [L(S)DA] within the linear muffin-tin orbital framework and the atomic spheres approximation report a fully gapped band structure at E_F ascribed to Kondo-like hybridization [26]. More interestingly, earlier LDA calculations using the linear augmented-plane-wave method report instead the opening of a pseudogap in the density of states [27]. The calculated Fermi surface consists of two electron pockets at the X point, i.e., in the node direction, and a holelike pocket in between the Γ and Y points. On the experimental side, core-level and resonant photoemission measurements show a mostly trivalent character for the Ce ions [28,29], although L_{III} absorption gives a slightly more

mixed value [30]. They additionally show a dominant Ni $3d$ -orbitals component and a Sn $5p$ -orbitals component in the conduction band [28,31]. A weak Ce $5d$ -orbitals contribution is also highlighted [32]. However, to the best of our knowledge, no experimental momentum-resolved study has ever been performed so far.

In the present work, we clarify the electronic structure of the conduction band and the Fermi surface of CeNiSn by directly accessing it with ARPES. At high temperature, before the Ce f level contributes, we observe that the conduction band forms quasi-one-dimensional Fermi sheets and one quasi-two-dimensional sheet. We discuss how anisotropic hybridization with a node along the a -axis can transform this quasi-two-dimensional sheet into a small relatively isotropic Fermi sheet compatible with SdH and with both the Nernst effect and magnetoresistance.

II. METHODS

A. Crystal

Crystals of CeNiSn possess a nonsymmorphic pattern in an orthorhombic structure. As depicted in Fig. 2(a), it consists of Ni and Sn ions forming a wobbling beehive net in the (b, c) plane, while Ce ions lodge at hexagon centers in between each Ni-Sn layer [33]. Single-crystal samples were grown using the Czochralski method as described in Ref. [7]. Figure 2(b) shows such a sample, with two perpendicular easy cleaving planes: Using single-crystal-transmitted x-ray diffraction with Rigaku's R-Axis RAPID II, we determined these planes to be equivalent (101) and $(10\bar{1})$ planes, as previously reported [34]. The obtained cleaved surface is represented by the b -axis in Fig. 2(c), next to the Brillouin zone in Fig. 2(d) oriented in a similar way.

B. Photoemission

Resonant PES measurements in Fig. 3 and ARPES measurements in Figs. 5 and 6 were performed at the Photon Factory end station BL-28A equipped with a Scienta SES-2002 analyzer. The samples were cooled down at a temperature of about 12 K, and the overall energy resolution was about 0.025 eV. ARPES measurements in Fig. 4 were performed at the BESSY-II endstation 1² equipped with a Scienta R8000 and a six-axis manipulator. The sample was cooled down at a temperature of 60 K and the overall energy resolution was

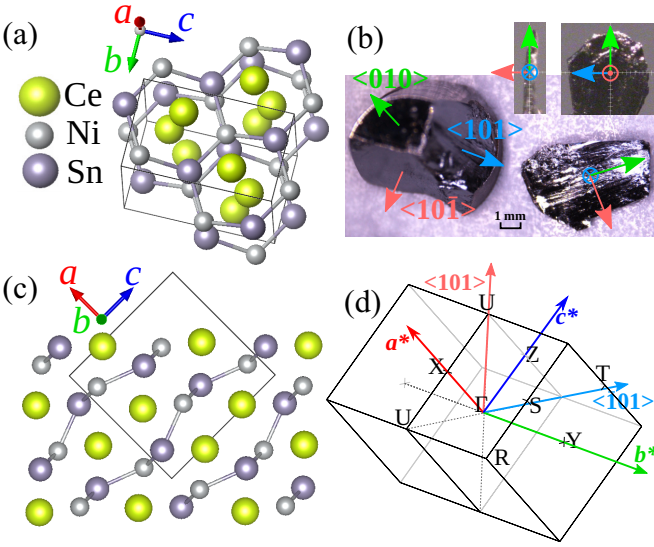


FIG. 2. (a) Representation of the crystal structure of CeNiSn. (b) Picture of an actual single crystal of CeNiSn, with cleaved pieces. Insets are displays of the crystal orientation made by Rigaku's RAXIS RAPID II. (c) Representation of a cleave (101) plane from the (010) axis. (d) CeNiSn Brillouin zone, with the $\langle 101 \rangle$ axis upward.

about 0.01 eV. All of the color-scale spectra of the main text are treated either by a second derivative or by two-dimensional (2D) curvature as described in Ref. [35]. Spectra from raw data can be found in the Supplemental Material [36].

C. Calculation

We have performed the band calculations employing the all-electron full-potential linearized augmented plane-wave (FLAPW) method, implemented in WIEN2K [37]. The generalized-gradient approximation (GGA) scheme is utilized for the DFT exchange-correlation functional [38], and the spin-orbit coupling (SOC) is included. We used an $18 \times 30 \times 18$ k -point mesh in the full Brillouin zone, and the product of R_{MT} and K_{max} was chosen as 8. This densely made k -point mesh is used for a comparison of the Fermi surface and the density plot between the results of experiment and calculation.

Open core calculation treats the level of f -electrons to be deep inside the core. This calculation simulates the high-temperature limit where f -electrons become incoherent and do not participate in electron hopping. With this calculation, the band structure of Ni d -electrons can be revealed, separated from the band structure of Ce f -electrons.

III. RESULTS

A. Resonant PES

Before mapping the band dispersion, we use the well-known Ce $4d \rightarrow 4f$ resonance [39] to separate the Ce $4f$ level from the conduction-band signal with the on- and off-resonance at 122 and 114 eV, respectively; see Fig. 3(a). The sharp Fano shape of this resonance, with its maximum at 122 eV, is visible in Fig. 3(c). The previously reported fine structure at 110 eV [29] is also visible. In addition

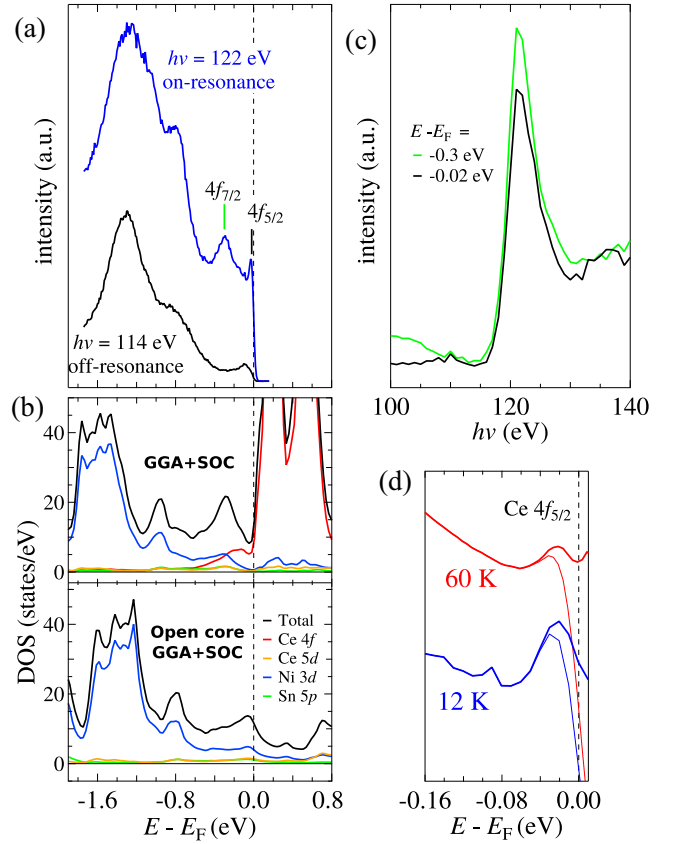


FIG. 3. (a) Ce $4d \rightarrow 4f$ resonant PES: On- and off-resonance spectra integrated around the normal emission at $T = 12$ K. (b) Total and partial density of states from GGA+SOC and Open core GGA+SOC calculations. See Sec. II for details about the calculations. (c) Photon energy dependence showing the Fano shape of the Ce $4d \rightarrow 4f$ resonance. (d) Close-up of the Ce $4f_{5/2}$ level divided by the Fermi-Dirac distribution at $T = 12$ and 60 K, to highlight its binding energy.

to confirming previous results, it allows us to identify the observed Ce f level and to suggest Open core calculation as a better basis to describe the conduction band.

As previously reported, we observe a wide structure at about 1 eV below E_{F} identified as part of the Ni $3d$ valence band, and the two spin-orbit-split Ce $4f$ levels visible on the on-resonance curve. An additional peak, part of the conduction band and visible on the off-resonance spectra, lies at about 0.09 eV below E_{F} . By looking closer at the Fermi level, Fig. 3(d), we surprisingly observe the Ce $4f_{5/2}$ peak lying 0.02 eV below E_{F} ; this cannot be the Kondo resonance peak, as was first expected. In fact, in the same way that the peak lying at about 0.3 eV below E_{F} is widely interpreted as a satellite of the spin-orbit-split Ce $4f_{7/2}$ level, the peak at 0.02 eV is most probably a satellite of the first CEF excited state. For Ce compounds, such a satellite has already been discussed in the case of CeSi₂ [40,41]. Moreover, it agrees with the CEF value extrapolated from INS measurements of doped samples [21,22]. The Kondo resonance peak should be observed closer to E_{F} with a temperature decrease through the onset of coherence at T_{coh} .

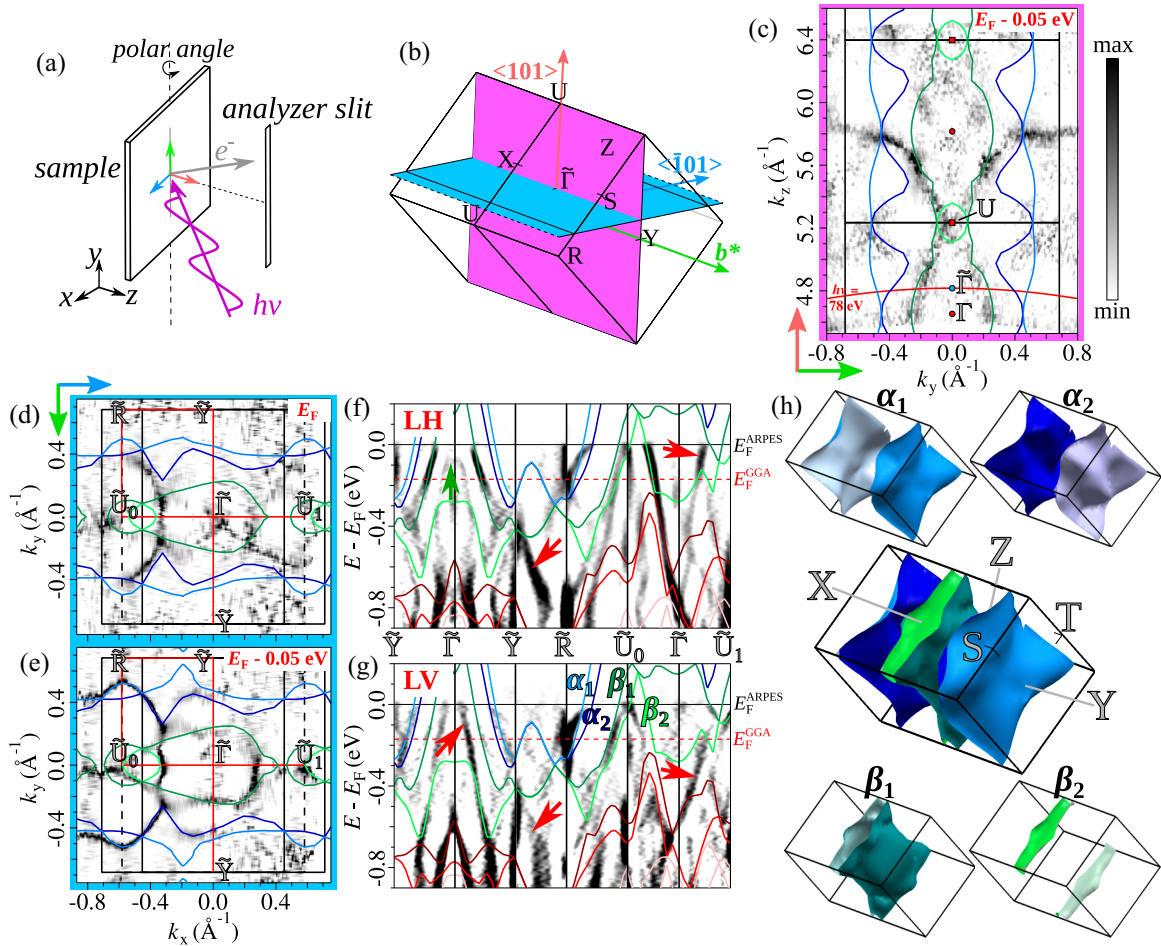


FIG. 4. (a) Brillouin-zone scheme. Photon energy dependence maps the red plane, while angular mapping of panels (d) and (e) is in the blue plane. (b) Photon energy dependence with the $\langle 010 \rangle$ direction along the analyzer slit. Inner potential is determined to be about $V_0 \approx 15$ eV. The red arc represents the position reached with $h\nu = 78$ eV. Colored lines are Open core GGA+SOC calculations. (c) Geometry of the measurements of this figure. (d) Angular mapping at the Fermi level with a constant photon energy of $h\nu = 78$ eV. Linear horizontal and vertical data have been summed up. Colored lines are Open core GGA+SOC calculations at E_F^{ARPES} . (e) Same 0.05 eV below the Fermi level. (f) Binding energy vs momentum cuts along the red line of panel (d), with linear horizontal polarization. (g) Same with linear vertical polarization. (h) Three-dimensional Fermi surface from Open core GGA+SOC calculations at E_F^{ARPES} .

As for previous DFT studies of CeNiSn, the Ce f band is much too wide in our GGA+SOC calculations, displayed in the upper part of Fig. 3(b), compared to the measurements of Fig. 3(a). As a consequence, the interacting conduction dispersion curves are strongly pushed down. On the other hand, by taking away the Ce $4f$ band, our Open core GGA+SOC calculations yield a density of states [lower part of Fig. 3(b)] that accounts better for the off-resonance PES measurements of Fig. 3(a). Open core calculations seem better suited for a comparison with ARPES measurements of the conduction band. This is confirmed by Fig. 4.

B. ARPES

1. 3D mapping

Figure 4 presents the three-dimensional mapping of the electronic structure of CeNiSn at $T = 60$ K. The $\langle 010 \rangle$ direction (green arrows) of the sample was aligned with the

analyzer slit, as shown by Fig. 4(a). Therefore, the intensity distribution of Fig. 4(c), obtained by tuning the photon energy from 70 to 160 eV, maps the red plane of Fig. 4(b). First of all, dispersions are visible along the momentum normal to the surface; this shows the bulk character of most of the observed bands. Due to symmetry consideration and a comparison with Open core GGA+SOC calculation (colored lines in the same figure), the inner potential was estimated to be $V_0 \approx 15$ eV. We performed polar angle mapping at a constant photon energy $h\nu = 78$ eV with both linear horizontal (LH) and linear vertical (LV) polarization. Figures 4(d) and 4(e) display the sum of these two polarizations at the Fermi energy E_F and 0.05 eV below it, respectively. It reaches a plane slightly above Γ , as shown by the red circle in Fig. 4(c) and the blue plane of Fig. 4(b). Following Figs. 4(f) and 4(g) are energy versus momentum cuts along the red lines of Figs. 4(d) and 4(e), from measurements performed with LH and LV polarized light, respectively. Colored lines superimposed on all the ARPES

data of this figure are Open core GGA+SOC calculations of CeNiSn. Relatively good agreement is found between ARPES and Open core GGA+SOC calculations. However, the observed Fermi level E_F^{ARPES} is 0.17 eV above the expected one, E_F^{GGA} , with the exception of a Π -shaped band observed at Γ with LH polarization. As shown by the green arrow, this Π -shaped band has its Fermi level at about E_F^{GGA} . Additional differences are described below. With the LV polarization, Fig. 4(g), instead of a Π -shaped band with a flat top, we observe a holelike dispersion that continues straight through the Fermi level. We believed this to be a surface state. Evidence for this claim is displayed and discussed in the Supplemental Material [36]. The same is true for the bands denoted by red arrows, as they can be found at a different k_z close to the Γ point. Despite the recent theory suggesting the existence of special topologically protected states at some surfaces of CeNiSn [25], the present work does not deal any further with surface states as the (101) cleaved surface is not subjected to any expectation of a topologically protected state.

In light of the exposed fairly good agreement between ARPES data and Open core GGA+SOC calculations, we can reasonably assume that the high-temperature Fermi surface of CeNiSn shares the same general shape as the calculated one at E_F^{ARPES} , Fig. 4(h). It is composed of four Fermi sheets that we label (from out to in) α_1 , α_2 , β_1 , and β_2 for convenience (corresponding band and Fermi momenta are labeled the same, for simplicity). They can be regrouped in two pairs, α_i (blue) and β_i (green), each pair being degenerate on the (100) and (001) Brillouin-zone edges. The outer pair, α_i , shows a quasi-one-dimensional character with the main dispersion along the b -axis, and, in view of its filling, it should be qualified as electronlike. The inner pair consists of a quasi-one-dimensional sheet β_1 and a quasi-two-dimensional sheet β_2 . The β_1 sheet also has its main dispersion along the b -axis, but it should be qualified as holelike. Finally, the β_2 sheet has a deformed tubelike shape, going along the X - U line, and it is also of holelike character. The highly anisotropic character of the presented Fermi surface could explain the 20-fold anisotropic magnetoresistance [12]. However, this scenario was discredited by the observation of an isotropic Nernst effect at low temperature. Section IV illustrates how the expected nodal hybridization can bring together the highly anisotropic Fermi surface at high temperature with the isotropic Nernst effect at low temperature.

Interestingly, even if the β_1 sheet has some closed orbits, a quantum oscillation signal from this Fermi surface configuration would be produced mostly by the β_2 sheet, with the magnetic field oriented in a solid angle around the c -axis; this is qualitatively similar to the experimental observations by SdH at low temperature [19,42]. Moreover, β_2 is the only Fermi sheet to cross the expected nodal line along the a -axis, i.e., the Γ - X line. This suggests that while other sheets will get fully gapped at low temperature, a sole pocket portion of β_2 will remain next to the X point. Again, this is in agreement with the description of a sole Fermi sheet by the same SdH measurements. In the following, we directly check by ARPES if β_2 is indeed the only Fermi sheet along the Γ - X line, and we determine its shape in the ΓXUZ plane.

2. Fermi sheet at the X point

Figure 5(a) shows a closeup of the dispersion at $\tilde{\Gamma}$ along the (010) direction, with an energy distribution curve (EDC) at normal emission: The Π -shaped band bounds at about 0.1 eV below E_F . By comparison with the calculation in Fig. 5(b), the α_i and β_1 bands have their Fermi level at E_F^{ARPES} , while the Π -shaped band β_2 has its Fermi level lowered to about E_F^{GGA} . If we assume a rigid band shift along the Γ - X line, then, according to our calculations, it will mean the existence of an additional pair of Fermi sheets centered at the X point, which we name $\{\delta_i\}_{i=1,2}$.

To precisely access the X point by ARPES, we need to map the (ΓXUZ) plane, shown in green in Fig. 5(c). To do so, the sample was oriented with the (101) direction along the analyzer slit, as shown in Fig. 5(d), and photon energy dependence was performed. The obtained intensity distribution mapping at E_F is plotted in Fig. 5(e). We then look at cuts along the U - X - U and Γ - X - Γ lines, Figs. 5(f) and 5(g), respectively. Our Open core GGA+SOC calculations are displayed in these figures with the E_F^{GGA} Fermi level in order to align with the binding energy of the β_2 band. The δ_i bands already seem to lie below the Fermi level at the X point. This is confirmed by the EDC of Fig. 5(h) integrated around the X point, in spite of the modest quality of the signal-to-noise ratio. Indeed, the EDC shows a local maximum below the Fermi level, even after division by the effective Fermi step (red curve). We fit this same EDC with Voigt profiles, i.e., Lorentzian profiles convoluted with a Gaussian to take into account the energy resolution, cut by the effective Fermi step. The fit of this EDC (blue curve) indicates the binding of the δ_i bands at 0.06 eV below the Fermi level. We can therefore conclude that there are no additional δ_i Fermi sheets, but only one Fermi sheet along the expected nodal line: β_2 .

3. Concave Fermi sheet

The Fermi momenta k_F^{ARPES} of the β_2 Fermi sheet are extracted from spectra at each measured photon energy and denoted in Fig. 6(a) by diamond markers. The intensity is not distributed symmetrically around the X point, most likely because of a strong matrix element. As a consequence, only one side of the Fermi sheet is visible, either below or above the U - X line. The underlying dispersions are visible on cuts parallel to the Γ - X line, integrated over the blue areas, and displayed in Figs. 6(b) and 6(c). For each of these spectra, a momentum distribution curve at the Fermi level is displayed to show the Fermi momenta. Figure 6(d) compares the symmetrized k_F^{ARPES} with our Open core GGA+SOC calculation. Around the U point, k_F^{ARPES} follows the calculated Fermi sheet at E_F^{GGA} . By going toward the X point, it shrinks to a value closer to the calculated Fermi sheet at E_F^{ARPES} . This behavior gives a concave shape to the measured Fermi sheet, similar to the description reported by SdH measurements [19].

IV. DISCUSSION

In this section, first we continue to suggest a comparison with SdH measurements. We also discuss how the expected nodal hybridization may shrink the β_2 sheet to a relatively isotropic Fermi sheet with highly anisotropic mass

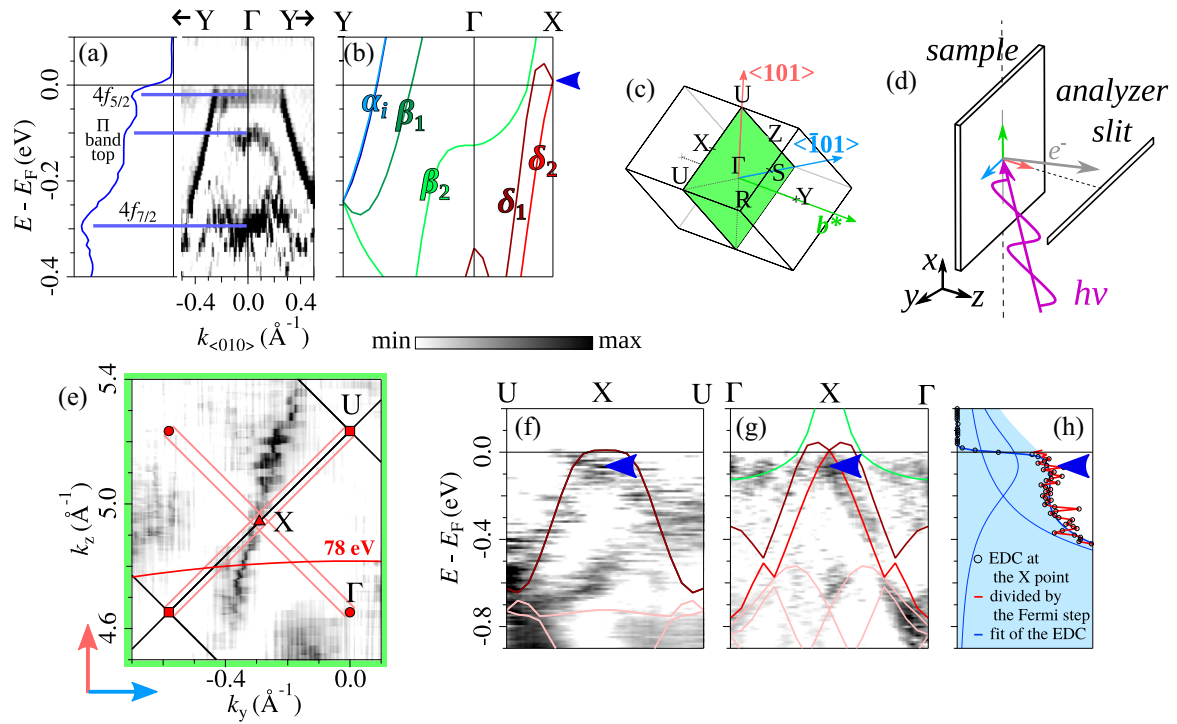


FIG. 5. (a) Cut along the $Y-\Gamma-Y$ line ($\langle 010 \rangle$) measured at 12 K and $h\nu = 78$ eV. The Π -shape band can be observed. The blue curve is an EDC at Γ . (b) Open core GGA+SOC calculation along the $Y-\Gamma-X$ line. (c) Brillouin-zone scheme. Here, photon energy dependence maps the green plane. (d) Geometry of the measurements of this figure. (e) Photon energy dependence measured with the analyzer slit aligned along the $\langle 101 \rangle$ direction, i.e., mapping of the ΓXUZ plane. The open rectangles indicate the ranges over which spectra of panels (g) and (h) have been integrated. (f) Binding energy vs momentum cut along the $U-X-U$ line. (g) Same along the $\Gamma-X-\Gamma$ line. (h) EDC at the X point (black open circles), integrated around the X point, divided by the effective Fermi-Dirac step in red. The bold blue curve is a fit of this EDC with two peaks, displayed with blue thin curves below. The blue area depicts the same fit, without the Fermi-Dirac cut.

distribution. Then, we discuss the remaining discrepancies overlooked by this work that will require further theoretical and experimental efforts in order to be clarified.

Figure 7(a) plots the cross-section area of Fermi sheets in \AA^{-2} on the left axis and the equivalent quantum oscillation frequency in units of T on the right axis versus the angle made by the normal to the cross section with the c -axis, as depicted by the three upper schemes. To estimate their area, the Fermi sheet cross sections are approximated to ellipses: with a short half-axis r and a long half-axis R , the ellipse area is equal to πrR . For the cross-section area indicated by the diamond markers, one half-axis is the distance from the X point to the Fermi momenta k_F^{ARPES} and the second half-axis is taken from the Open core GGA+SOC calculation (at E_F^{ARPES}) along the $X-S$ line. The same is done to draw the black line with Fermi momenta obtained by fitting k_F^{ARPES} with a power law, and to draw the green line from our Open core GGA+SOC calculations. Because of its concave shape, the cross section of the β_2 Fermi sheet increases with the angle faster than for a bidimensional Fermi sheet. As we noted in the previous section, this is in accordance with the observation from SdH data [19] reproduced here by the full pink circles. Yet, the cross-section area extracted from ARPES at high temperature and Open core GGA+SOC calculation is greater than the SdH frequencies measured at low temperature by a factor of about 3. The nodal hybridization scenario can account for this difference. Indeed, when lowering the temperature, the Fermi momentum of a holelike band remains unchanged along the

nodal line, while it shrinks in other directions, as we already described in Fig. 1(c). Therefore, we expect the β_2 sheet to remain the same along the $\Gamma-X$ line (i.e., the nodal line) but to shrink along the $X-S$ line. In a solid angle around the nodal line, the β_2 sheet would conserve its concave shape, and its cross section would simply be reduced by the same factor as the Fermi momenta along the $X-S$ line. The blue area in Fig. 7(b) illustrates this hypothetical low-temperature reduced Fermi sheet. The corresponding reduced cross section, represented by the blue line and markers in the lower part of Fig. 7(a), shows good agreement with the SdH data. This means that the concavity observed by ARPES is quantitatively similar to that reported by SdH. At the same time, the β_2 sheet would also shrink along the $X-U$ line, potentially going from its anisotropic quasi-two-dimensional shape to a relatively isotropic shape. As illustrated by Fig. 7(c), this would imply an extremely heavy effective mass along the $X-U$ line, while the mass remains rather light along the nodal line.

The three characteristics we just described tend to ensure that our hypothetical low-temperature Fermi sheet would be compatible with previous experimental works: Its closed, mostly isotropic shape makes it compatible with Nernst effect measurements; its highly anisotropic mass distribution makes it compatible with anisotropic magnetoresistance; and its concave shape makes it compatible with SdH measurements.

Finally, in the Introduction of this article, we described how previous interpretations concluded from the sign of the Hall coefficient that the Fermi sheet measured by SdH should

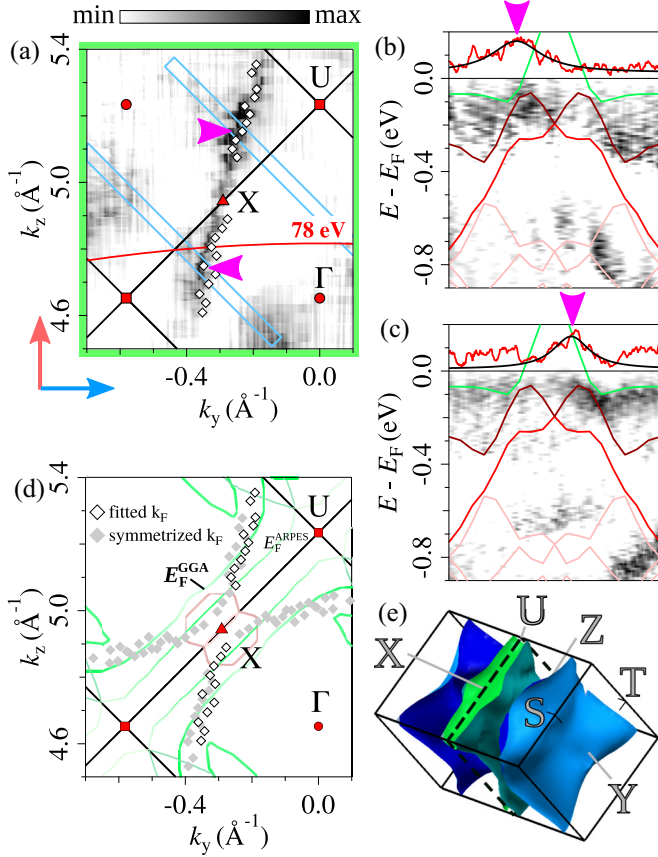


FIG. 6. (a) Same as Fig. 5(e). The open rectangles indicate the ranges over which spectra of panels (b) and (c) have been integrated. Diamond markers are Fermi momentum extracted from ARPES, k_F^{ARPES} . (b),(c). Binding energy vs momentum cuts along lines parallel to the Γ -X- Γ line, as can be seen in panel (a). (d) Fermi momenta from ARPES are symmetrized around the X point. Bold colored lines are Open core GGA+SOC calculations at E_F^{GGA} , while thin colored lines are the same calculation at E_F^{ARPES} . (e) 3D Fermi surface from Open core GGA+SOC calculations at E_F^{ARPES} . The black broken lines indicate the plane cut by panel (d).

be electronlike. Indeed, as the anomalous Hall effect is suppressed at low temperature [4], below 4 K the Hall coefficient finally becomes negative in all configurations [43,44]. Naively, this indicates that the carriers of the semimetallic phase of CeNiSn are electrons. However, from combined ARPES measurements and Open core GGA+SOC calculations, our work indicates a holelike band in the direction of the expected nodal line in the high-temperature regime. While this Fermi sheet is identified from its shape as the one measured by SdH, it is unlikely that it becomes an electronlike pocket at low temperature.

Two hypotheses should be considered. First, because of the highly anisotropic velocity along our hypothetical Fermi sheet and its particular shape mixing concave and convex segments, the interpretation of the Hall coefficient is not trivial. As described by Ong in Ref. [45], the concave segment with high velocity contributes negatively to the Hall conductivity: it may cause the Hall coefficient to be negative. Second, as was already mentioned in the Introduction of this article, the existence of an additional heavier Fermi sheet is already

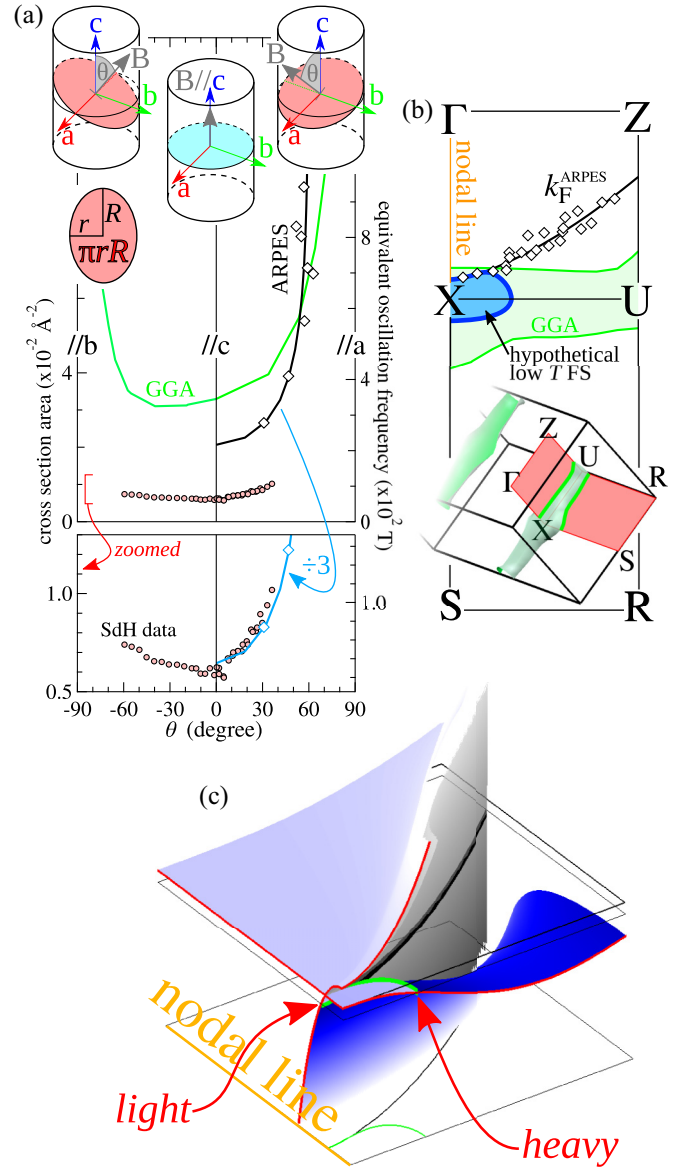


FIG. 7. (a) Angle-dependent area cross section of the calculated and measured β_2 Fermi sheet. The equivalent oscillation frequency is displayed on the right axis of the graph in units of T. The SdH data extracted from Ref. [19] are reproduced by the full pink circle markers. (b) Representation of the calculated and measured β_2 Fermi sheet in the ΓXUZ and $XSRU$ planes. The black curve is a power fit of k_F^{ARPES} . The blue area is a sketch of the hypothetical low-temperature Fermi sheet after the expected nodal hybridization is turned on, with the nodal line being the Γ -X line, here in orange. (c) Simplified sketch of how the nodal hybridization may take place with a concave quasi-2D Fermi sheet. We see how the low-temperature Fermi sheet is light along the nodal line but very heavy in the other direction.

suggested by the Sommerfeld coefficient and should not be overlooked. In fact, one should take a closer look at the symmetry of the Ce 4f ground state determined experimentally by polarization-dependent x-ray absorption spectroscopy [17]. It points to the ground-state theoretically defined by Moreno *et al.* [15]. With this symmetry, in addition to the nodal line along the a -axis, the hybridization potential is also almost

suppressed along the (011) direction. From the high-temperature conduction band depicted by the present work, this would likely mean the formation by hybridization of the α_i bands of two heavy electronlike Fermi sheets around the T point. Such a hypothesis can only be checked by low-temperature ARPES measurements.

V. CONCLUSIONS

At first, resonant-PES allows us to observe the Ce f level, and to suggest that the Open core GGA+SOC calculation provides a better description of the measured density of states. Thanks to further fairly good agreement between our calculations and our high-temperature ARPES measurements, we are able to depict the basic shape of the high-temperature Fermi surface of CeNiSn. It is composed of highly anisotropic sheets that first appear to be in contradiction with recent isotropic Nernst effect measurements. Additional ARPES measurements show that only one Fermi sheet, β_2 , is located in the direction of the expected hybridization node. We further reveal the concave shape of the β_2 Fermi sheet, similar to the description by SdH measurements. We then discuss how the effect of the expected anisotropic hybridization may settle the dichotomy between the low-temperature Nernst effect by the transformation of the observed β_2 Fermi sheet into a nearly isotropic pocket with highly anisotropic effective masses, also compatible with low-temperature magnetoresistance and SdH measurements.

Finally, we discuss the negative sign of the Hall coefficient, which, if we follow the conclusion of the SdH study of Ref. [19], first seems to be in contradiction with the holelike character of our hypothetical low-temperature Fermi sheet. While the anisotropy and peculiar shape of this last may give a negative contribution to the Hall coefficient, the existence of an additional Fermi sheet is a likely hypothesis, as already suggested by the unaccounted Sommerfeld coefficient.

Only a direct probe will settle this question. It calls for highly resolved ARPES measurements well below the coherence temperature where the gap is fully open, in the surrounding of both the X and T points. The present work serves as a solid basis for these challenging measurements, thanks to a wide view of the CeNiSn conduction band over most of the Brillouin zone, and to precise suggestions of relevant loci.

All data generated during this study are available from the corresponding author upon reasonable request.

ACKNOWLEDGMENTS

We thank P. Coleman and P. Goddard for very helpful discussions. We thank HZB for the allocation of synchrotron radiation beamtime, and we gratefully acknowledge the financial support by HZB. This work was supported by the JSPS KAKENHI (Grants No. JP18H01165 and No. JP19F19030). T.-S.N. and B.I.M. acknowledge the support from the NRF Korea (No. 2017R1A2B4005175).

-
- [1] K. Izawa, T. Suzuki, T. Fujita, T. Takabatake, G. Nakamoto, H. Fujii, and K. Maezawa, *Phys. Rev. B* **59**, 2599 (1999).
 - [2] K. Izawa, T. Suzuki, T. Fujita, T. Takabatake, G. Nakamoto, H. Fujii, and K. Maezawa, *J. Magn. Magn. Mater.* **177-181**, 395 (1998), International Conference on Magnetism.
 - [3] T. Takabatake, H. Tanaka, Y. Bando, H. Fujii, S. Nishigori, T. Suzuki, T. Fujita, and G. Kido, *Phys. Rev. B* **50**, 623 (1994).
 - [4] T. Takabatake, M. Nagasawa, H. Fujii, M. Nohara, T. Suzuki, T. Fujita, G. Kido, and T. Hiraoka, *J. Magn. Magn. Mater.* **108**, 155 (1992).
 - [5] T. Takabatake, Y. Nakazawa, and M. Ishikawa, *Jpn. J. Appl. Phys.* **26**, 547 (1987).
 - [6] T. Takabatake, F. Teshima, H. Fujii, S. Nishigori, T. Suzuki, T. Fujita, Y. Yamaguchi, J. Sakurai, and D. Jaccard, *Phys. Rev. B* **41**, 9607 (1990).
 - [7] G. Nakamoto, T. Takabatake, H. Fujii, A. Minami, K. Maezawa, I. Oguro, and A. Menovsky, *J. Phys. Soc. Jpn.* **64**, 4834 (1995).
 - [8] M. Kyogaku, Y. Kitaoka, H. Nakamura, K. Asayama, T. Takabatake, F. Teshima, and H. Fujii, *J. Phys. Soc. Jpn.* **59**, 1728 (1990).
 - [9] K. Nakamura, Y. Kitaoka, K. Asayama, T. Takabatake, H. Tanaka, and H. Fujii, *J. Phys. Soc. Jpn.* **63**, 433 (1994).
 - [10] T. Ekino, T. Takabatake, H. Tanaka, and H. Fujii, *Phys. Rev. Lett.* **75**, 4262 (1995).
 - [11] D. N. Davydov, S. Kambe, A. G. M. Jansen, P. Wyder, N. Wilson, G. Lapertot, and J. Flouquet, *Phys. Rev. B* **55**, R7299 (1997).
 - [12] Y. Inada, T. Ishida, H. Azuma, D. Aoki, R. Settai, Y. Ōnuki, K. Kobayashi, T. Takabatake, G. Nakamoto, H. Fujii, and K. Maezawa, *Physica B* **230-232**, 690 (1997), Proceedings of the International Conference on Strongly Correlated Electron Systems.
 - [13] Yu. Kagan, K. A. Kikoin, and N. V. Prokof'ev, *Pis'ma Zh. Eksp. Teor. Fiz.* **57**, 584 (1993) [*JETP Lett.* **57**, 600 (1993)].
 - [14] H. Ikeda and K. Miyake, *J. Phys. Soc. Jpn.* **65**, 1769 (1996).
 - [15] J. Moreno and P. Coleman, *Phys. Rev. Lett.* **84**, 342 (2000).
 - [16] M. Miyazawa and K. Yamada, *J. Phys. Soc. Jpn.* **72**, 2033 (2003).
 - [17] F. Strigari, Ph.D. thesis, Universität zu Köln, 2015.
 - [18] U. Stockert, P. Sun, N. Oeschler, F. Steglich, T. Takabatake, P. Coleman, and S. Paschen, *Phys. Rev. Lett.* **117**, 216401 (2016).
 - [19] T. Terashima, C. Terakura, S. Uji, H. Aoki, Y. Echizen, and T. Takabatake, *Phys. Rev. B* **66**, 075127 (2002).
 - [20] Y. Kagan, K. A. Kikoin, and A. S. Mishchenko, *Phys. Rev. B* **55**, 12348 (1997).
 - [21] J.-Y. So, S.-J. Oh, J.-G. Park, D. T. Adroja, K. A. McEwen, and T. Takabatake, *Phys. Rev. B* **71**, 214441 (2005).
 - [22] D. Adroja, B. Rainford, A. Neville, and A. Jansen, *Physica B* **223-224**, 275 (1996), Proceedings of the International Conference on Strongly Correlated Electron Systems.
 - [23] M. Dzero, K. Sun, V. Galitski, and P. Coleman, *Phys. Rev. Lett.* **104**, 106408 (2010).
 - [24] M. Dzero, J. Xia, V. Galitski, and P. Coleman, *Annu. Rev. Condens. Matter Phys.* **7**, 249 (2016).

- [25] P.-Y. Chang, O. Erten, and P. Coleman, *Nat. Phys.* **13**, 794 (2017).
- [26] T. J. Hammond, G. A. Gehring, M. B. Suvasini, and W. M. Temmerman, *Phys. Rev. B* **51**, 2994 (1995).
- [27] A. Yanase and H. Harima, *Prog. Theor. Phys. Suppl.* **108**, 19 (1992).
- [28] S. Nohara, H. Namatame, A. Fujimori, and T. Takabatake, *Phys. Rev. B* **47**, 1754 (1993).
- [29] J.-S. Kang, C. G. Olson, Y. Inada, Y. Ōnuki, S. K. Kwon, and B. I. Min, *Phys. Rev. B* **58**, 4426 (1998).
- [30] P. Alekseev, E. Klement'ev, V. Lazukov, E. Nefedova, I. Sadikov, M. Khlopkin, A. Y. Muzychka, I. Sashin, N. Efreмова, and W. Bühner, *Zh. Eksp. Teor. Fiz.* **106**, 1228 (1994) [*J. Exp. Theor. Phys.* **79**, 665 (1994)].
- [31] A. Sekiyama, Y. Fujita, M. Tsunekawa, S. Kasai, A. Shigemoto, S. Imada, D. Adroja, T. Yoshino, F. Iga, T. Takabatake, T. Nanba, and S. Suga, *J. Electron Spectrosc. Relat. Phenom.* **144-147**, 655 (2005), Proceeding of the Fourteenth International Conference on Vacuum Ultraviolet Radiation Physics.
- [32] A. Sekiyama, S. Suga, T. Iwasaki, S. Ueda, S. Imada, Y. Saitoh, T. Yoshino, D. Adroja, and T. Takabatake, *J. Electron Spectrosc. Relat. Phenom.* **114-116**, 699 (2001), Proceeding of the Eight International Conference on Electronic Spectroscopy and Structure.
- [33] I. Higashi, K. Kobayashi, T. Takabatake, and M. Kasaya, *J. Alloys Compd.* **193**, 300 (1993), Proceedings of the International Conference, Rare Earths '92.
- [34] T. Suzuki, M. Nohara, S. Fujisawa, H. Fujisaki, T. Fujita, M. Nagasawa, T. Takabatake, and H. Fujii, *J. Magn. Magn. Mater.* **104-107**, 1293 (1992), Proceedings of the International Conference on Magnetism, Part II.
- [35] P. Zhang, P. Richard, T. Qian, Y.-M. Xu, X. Dai, and H. Ding, *Rev. Sci. Instrum.* **82**, 043712 (2011).
- [36] See Supplemental Material at <http://link.aps.org/supplemental/10.1103/PhysRevB.100.045133> for the raw data of all curvatures and second derivatives used in this article, and for a discussion on the surface character of the band observed above the Π -shaped band.
- [37] P. Blaha, K. Schwarz, G. K. H. Madsen, D. Kvasnicka, J. Luitz, R. Laskowski, F. Tran, and L. D. Marks, *WIEN2k, An Augmented Plane Wave + Local Orbitals Program for Calculating Crystal Properties* (Karlheinz Schwarz, Techn. Universität Wien, Austria, 2018).
- [38] J. P. Perdew, K. Burke, and M. Ernzerhof, *Phys. Rev. Lett.* **77**, 3865 (1996).
- [39] J. W. Allen, S. J. Oh, O. Gunnarsson, K. Schönhammer, M. B. Maple, M. S. Torikachvili, and I. Lindau, *Adv. Phys.* **35**, 275 (1986).
- [40] F. Patthey, J.-M. Imer, W.-D. Schneider, H. Beck, Y. Baer, and B. Delley, *Phys. Rev. B* **42**, 8864 (1990).
- [41] S. Hüfner, in *Photoelectron Spectroscopy—Principles and Applications*, 3rd ed., edited by Springer (Springer-Verlag, Berlin Heidelberg, 2003), Vol. 1.
- [42] T. Terashima, C. Terakura, S. Uji, H. Aoki, Y. Echizen, and T. Takabatake, *Physica B* **329-333**, 535 (2003), Proceedings of the 23rd International Conference on Low Temperature Physics.
- [43] T. Takabatake, G. Nakamoto, M. Sera, K. Kobayashi, H. Fujii, K. Maezawa, I. Oguro, and Y. Matsuda, *J. Phys. Soc. Jpn.* **65**, Suppl. B, 105 (1996).
- [44] T. Takabatake, F. Iga, T. Yoshino, Y. Echizen, K. Katoh, K. Kobayashi, M. Higa, N. Shimizu, Y. Bando, G. Nakamoto, H. Fujii, K. Izawa, T. Suzuki, T. Fujita, M. Sera, M. Hiroi, K. Maezawa, S. Mock, H. Löhneysen, A. Brückl, K. Neumaier, and K. Andres, *J. Magn. Magn. Mater.* **177-181**, 277 (1998), international Conference on Magnetism.
- [45] N. P. Ong, *Phys. Rev. B* **43**, 193 (1991).